Time-resolved electron $(e,2e)$ momentum spectroscopy: Application to laser-driven electron population transfer in atoms

Hua-Chieh Shao* and Anthony F. Starace†
Department of Physics and Astronomy, University of Nebraska, Lincoln, Nebraska 68588-0299, USA

(Received 1 December 2017; published 5 February 2018)

Owing to its ability to provide unique information on electron dynamics, time-resolved electron momentum spectroscopy (EMS) is used to study theoretically a laser-driven electronic motion in atoms. Specifically, a chirped laser pulse is used to adiabatically transfer the populations of lithium atoms from the ground state to the first excited state. During this process, impact ionization near the Bethe ridge by time-delayed ultrashort, high-energy electron pulses is used to image the instantaneous momentum density of this electronic population transfer. Simulations with 100 fs and 1 fs pulse durations demonstrate the capability of EMS to image the time-varying momentum density, including its change of symmetry as the population transfer progresses. Moreover, the spectra corresponding to different pulse durations reveal different kinds of electronic motion. We discuss how to properly interpret these time-resolved EMS spectra, which represent a generalization of time-independent EMS.

DOI: 10.1103/PhysRevA.97.022702

I. INTRODUCTION

Studies of time-resolved electron dynamics in various atomic, molecular, and condensed-matter reactions have increased over the past two decades [1–7] owing to experimental progress in generating ultrashort and/or intense pulses of extreme ultraviolet light [8,9], x rays [10,11], and electrons [12,13]. These advances open the possibility of obtaining a deeper understanding of physical and chemical reaction mechanisms. In particular, electronic motions during reactions have been monitored in real time [14–16]. Moreover, various aspects of electronic motions can be retrieved using different probe schemes. For example, attosecond transient absorption spectroscopy tracks the frequencies, phases, and lifetimes of excited oscillating dipoles [17,18], time-resolved x-ray absorption and x-ray Raman spectroscopy provide element-specific probes of evolving electronic motion and chemical bonding [19,20], and x-ray and electron diffraction are able to directly image electronic spatial motions with (sub)angstrom resolution [21–23].

Electron momentum spectroscopy (EMS) provides a different probe scheme that images electronic states in *momentum* space [24–28]. It thus provides a distinct yet complementary perspective on electron dynamics. In brief, EMS utilizes the clean knockout mechanism of high-energy impact ionization near the Bethe ridge [29], whereby the ionized electron receives nearly all of the momentum transfer from the projectile electron (with the target ion nuclei and electrons serving as spectators whose only role is to define the binding energy of the ionized electron). Hence this impact ionization process is essentially a binary collision between the projectile electron and the target electron that is ionized. By measuring the momenta of the two outgoing electrons, one can infer the momentum of the ionized electron and its momentum distribution at the instant of collision using the conservation laws of energy and momentum and the differential ionization cross section. The binary collision approximation is most valid for weakly bound electrons. Hence EMS is most useful for determining the momentum density of valence electrons, which usually play dominant roles in chemical bonds and reactions. Moreover, EMS measurements having sufficient energy resolution enable state-selective determination of the target electron(s) participating in a reaction. More importantly, EMS renders a straightforward interpretation of the experimental results, without further reference to simulations and/or elaborate analyses. The main disadvantage of EMS is that it suffers from low data statistics due to small cross sections [25].

Early research on the electron impact ionization process, or $(e,2e)$, for the case of high-energy incident electrons was focused on the ionization mechanism and the validity of the momentum-density interpretation for target valence electronic states (see, e.g., Refs. [30–32]). The ability of EMS to map momentum densities was beautifully demonstrated for hydrogen and helium electronic orbitals [33,34]. Over the past three decades EMS experimental techniques have steadily improved the precision, accuracy, and detection efficiency of EMS measurements [25,28]. As a result, EMS measurements have been employed as benchmarks for evaluating the accuracy of theoretical calculations of molecular momentum distributions [35,36]. Moreover, owing to the sensitivity of valence electrons to the structure of a molecule, EMS can detect and study modifications of electron momentum densities due to molecular conformation changes [37], molecular pseudorotations [38], multicenter effects [39,40], or vibrations [41,42]. Recently, $(e,2e)$ measurements have been carried out for excited molecular states [43,44]. Recent theoretical advances include analyses and simulations of laser-assisted EMS processes [45] as well as of time-resolved EMS for electronic motions in atoms and molecules [46]. With regard to the latter, the time scale of typical electronic motions ranges from femtosecond (fs) to sub-fs, which exceeds current temporal resolutions of EMS measurements.

*hcshao@huskers.unl.edu
†astarace1@unl.edu

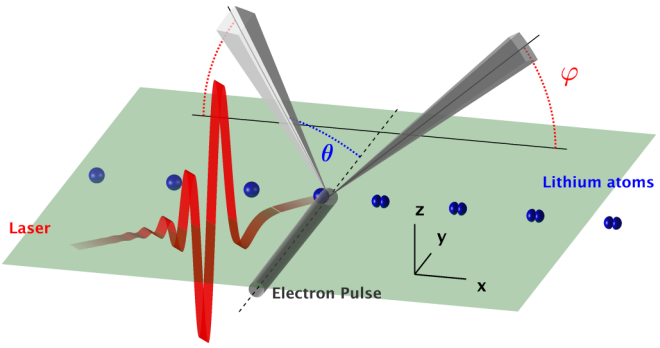

FIG. 1. Schematic setup for time-resolved electron momentum spectroscopy (EMS) for a laser-driven population transfer in lithium atoms. A chirped laser pulse drives the population of the lithium atoms adiabatically from their ground state ($2s$) to their first excited state ($2p$). During this transition, changes in the population and symmetry of the valence electron's momentum density are imaged by time-delayed, high-energy electron pulses through the mechanism of electron impact ionization, i.e., $(e,2e)$. In the symmetric noncoplanar configuration, the scattered and ejected electrons share the same kinetic energy, scattering angle θ, and azimuthal detection angle φ (relative to the positive and negative x axis). By varying the azimuthal angle φ of both detectors, the momentum distribution of the orbital from which the electron is ionized can be mapped from the EMS spectrum. The scattering angle θ is chosen such that the momentum density along the z axis is imaged. For future reference, the coordinate system used in this paper is defined here.

In this paper we propose use of EMS to image a laser-controlled, picosecond (ps) electronic motion in atoms as a means of exploring the capabilities and limitations of EMS for studying time-resolved electron dynamics. Specifically, we consider a laser-driven population transfer in lithium atoms from the ground state ($2s$) to the first excited state ($2p$) [47]. This electronic motion comprises two distinct time scales. The slow population transfer motion is controlled by the driving laser, while the fast motion stems from the quantum beating of the coherent eigenstates involved in the population transfer. The symmetric noncoplanar electron detection configuration shown in Fig. 1 is chosen for EMS measurements because this setup selects impact ionization events that satisfy the clean knockout mechanism and because the differential cross section directly reflects the momentum distribution of the lithium valence electronic state.

We model the time-resolved EMS spectra by generalizing the time-independent theory of EMS to take account of the effects of the driving laser field and the finite duration of the incident electron pulses (Sec. II). Simulations with two pulse durations (100 fs and 1 fs) are performed (Sec. III). The simulations show that the time-resolved spectra depend critically on the pulse duration and that different kinds of information on the electronic motion can be retrieved from the different spectra (Sec. IV). The results and analyses presented here thus extend the conventional momentum-density interpretation of the EMS spectra to the case of time-resolved EMS, which we demonstrate to be an effective tool for directly investigating electron dynamics in atoms and molecules.

Finally, we note that x-ray Compton scattering provides a similar probe scheme for measuring the momentum density of target electrons [48,49]. However, as discussed above, EMS requires the clean knockout mechanism involving large momentum transfers as well as a coincidence measurement that resolves the momenta of both the scattered particle (i.e., either the incident electron or the incident x-ray photon) and the ejected electron. These requirements can be challenging for x-ray Compton experiments.

II. THEORY

In this section we present the theory upon which we base our simulations of time-dependent EMS of a laser-driven adiabatic $2s \rightarrow 2p$ population transfer in Li atoms. In Sec. II A we recapitulate the conventional theory of time-independent EMS, using lithium as an example and with an emphasis on how and under what conditions the momentum densities of target stationary states relate to $(e,2e)$ measurements. In Sec. II B we then compare the conventional theory with the time-dependent theory, with a focus on the additional conditions required when making time-resolved measurements. Finally, in Sec. II C we briefly discuss the adiabatic passage theory as applied to frequency-swept population transfer in a two-state, lithium atom system. Unless specified otherwise, atomic units (a.u.), $e = \hbar = m_e = 1$, are used throughout this paper.

A. Electron momentum spectroscopy

Consider an impact ionization process in which an energetic electron collides with a lithium atom,

$$e^-(\boldsymbol{k}_0) + \mathrm{Li}(\boldsymbol{k}_1) \rightarrow e^-(\boldsymbol{k}_a) + e^-(\boldsymbol{k}_b) + \mathrm{Li}^+(\boldsymbol{k}_c)\,, \qquad (1)$$

where $\boldsymbol{k}_0$ and $\boldsymbol{k}_1$ are the respective momenta of the incident electron and the lithium atom and $\boldsymbol{k}_a$, $\boldsymbol{k}_b$, and $\boldsymbol{k}_c$ are the momenta of the scattered electron, the ejected electron, and the residual ion, respectively. We assume that the momenta of the incident electron and the lithium atom target are well defined (i.e., that they can be characterized by a single value). If the momenta of the projectile electron and the lithium atom have finite distributions, these are treated as probability distributions rather than as coherent (wave-packet) distributions.

The collision ionizes the lithium atom from an initial eigenstate ϕ_n to an ionic eigenstate ϕ_m^{-1} and the corresponding transition amplitude is [25,26,50,51]

$$T_{mn} = \left(\chi_a^{(-)}\,\chi_b^{(-)}\,\chi_c^{(-)}\,\phi_m^{-1}, V\,\psi_n^{(+)}\right), \qquad (2)$$

where the $\chi_j^{(-)}$, $j \in \{a,b,c\}$, are eigenstates of the particles on the right-hand side of Eq. (1), V is the Coulomb interaction between the incident electron and the ionized electron, and $\psi_n^{(+)}$ is the scattering state corresponding to the left-hand side of Eq. (1). Here n and m denote the collections of quantum numbers specifying the neutral and ionic states of the lithium atom, respectively. The superscripts $(+)$ and $(-)$ for the entrance state $\psi_n^{(+)}$ and the exit states $\chi_j^{(-)}$ indicate respectively outgoing- and incoming-wave boundary conditions. Note that a δ function for the conservation of energy has been factored out from Eq. (2).

In general, the evaluation of the transition amplitude T_{mn} is challenging because the scattering state $\psi_n^{(+)}$ can involve complicated electron correlations during the process of ionization [52]. However, under the so-called EMS conditions

[25,26,28], as discussed below, the ionization mechanism simplifies dramatically, and, as a result, the calculation becomes much simpler. Moreover, the final expression yields a clear physical interpretation. *First*, for energetic collisions the distortion of the wave functions of the incident electron and of the lithium atom target can be neglected, so that the first-order Born approximation can be employed for the projectile-target interaction. Hence $\psi_n^{(+)}$ can be approximated by the product of the initial states,

$$\psi_n^{(+)} \simeq \chi_0\, \chi_1\, \phi_n\,, \tag{3}$$

where χ_0 and $\chi_1\, \phi_n$ are respectively the states of the incident electron and the lithium atom target. Since we assume the incident electron is characterized by a single momentum, χ_0 is a plane wave with momentum $\boldsymbol{k}_0$,

$$\chi_0 = (2\pi)^{-3/2}\, e^{i\boldsymbol{k}_0\cdot\boldsymbol{x}_0}, \tag{4}$$

where $\boldsymbol{x}_0$ is the coordinate of the incident electron. Likewise, χ_1 has a similar plane-wave expression with momentum $\boldsymbol{k}_1$. *Second*, since EMS measurements select ionization events with large momentum transfer, both the ejected electron and the scattered electron have large kinetic energy. Therefore, the distortion of the exit states after the collision is also small and the exit states can also be approximated by plane waves,

$$\chi_j^{(-)} \simeq (2\pi)^{-3/2}\, e^{i\boldsymbol{k}_j\cdot\boldsymbol{x}_j}, \tag{5}$$

where $\boldsymbol{x}_j$ is the coordinate of the jth particle, $j \in \{a,b,c\}$. While Eq. (5) may seem to be a crude approximation for particles having Coulomb interactions, simulations have shown that calculations using the plane-wave approximation agree with those using the distorted-wave approximation provided that large momenta are transferred and that the initial momentum of the ionized electron at the instant of collision is $\lesssim$1.5 a.u. (i.e., near the Bethe ridge) [28,53]. The validity of this plane-wave approximation can also be verified experimentally by comparing (e, 2e) measurements for different energies of the incident electrons (see, e.g., Refs. [28,35,37,38]). Since we are interested in the motion of valence electrons, whose momentum distributions are typically concentrated within the range of 0.0–2.0 a.u., this approximation is adequate for our purposes. *Third*, owing to the heaviness of the Li nucleus, the electron-to-nucleus mass ratio is assumed to be negligible. Under the above considerations, the ionization amplitude T_{mn} factorizes into a product of kinetic and structural factors [25,26]:

$$T_{mn} \simeq \delta(\mathcal{P}_f - \mathcal{P}_i)\, \frac{1}{2\pi^2}\, \frac{1}{\boldsymbol{s}^2}\, \psi_{mn}(\boldsymbol{q}). \tag{6}$$

Here $\mathcal{P}_f \equiv \boldsymbol{k}_a + \boldsymbol{k}_b + \boldsymbol{k}_c$ and $\mathcal{P}_i \equiv \boldsymbol{k}_0 + \boldsymbol{k}_1$ are the respective linear momenta of the products and reactants, $\boldsymbol{s} \equiv \boldsymbol{k}_0 - \boldsymbol{k}_a$ is the momentum transfer, $\boldsymbol{q} \equiv \boldsymbol{k}_a + \boldsymbol{k}_b - \boldsymbol{k}_0$, and $\psi_{mn}(\boldsymbol{q})$ is the structure amplitude [26], given by

$$\psi_{mn}(\boldsymbol{q}) = \frac{1}{(2\pi)^{3/2}} \int d\boldsymbol{x}_b\, e^{-i\boldsymbol{q}\cdot\boldsymbol{x}_b} \left(\phi_m^{-1}, \phi_n\right). \tag{7}$$

The inner product in the integrand of Eq. (7) involves an integration over all coordinates of the target electrons except for the coordinate $\boldsymbol{x}_b$ of the ejected electron. The structure amplitude $\psi_{mn}(\boldsymbol{q})$ in Eq. (7) is the Fourier transform of the overlap between the ionic and neutral states of the lithium atom, which is a single-electron function called the Dyson orbital.

The structure amplitude can be further related to the momentum wave function of the orbital from which the valence electron is ejected by making some additional approximations. Specifically, if a single Slater determinant is used to construct each of the eigenstates ϕ_n and ϕ_m^{-1}, then the Dyson orbital is the ejected electron's momentum space wave function multiplied by a spectroscopic factor, i.e., the overlap of the core electrons' initial and final orbitals. If one further assumes that the collision does not excite the core electrons and that the core orbitals do not relax during the ejection of the valence electron, then the frozen-core approximation can be used. In this case, the spectroscopic factor is unity. Consequently, the Dyson orbital is simply the momentum space wave function of the valence (ejected) electron. The above assumptions can be satisfied by selecting collision events near the Bethe ridge having large momentum transfer.

For given initial and final states, ϕ_n and ϕ_m^{-1}, of the lithium atom and ion, EMS simulations usually calculate the triply differential cross section, $d^3\sigma/dE_a\, d\hat{\boldsymbol{k}}_a\, d\hat{\boldsymbol{k}}_b$, corresponding to the scattering of the incident electron with energy E_a along the angle $\hat{\boldsymbol{k}}_a$ and the ionized electron escaping along the angle $\hat{\boldsymbol{k}}_b$. The triply differential cross section is proportional to the absolute square of the transition amplitude T_{mn}:

$$\frac{d^3\sigma}{dE_a\, d\hat{\boldsymbol{k}}_a\, d\hat{\boldsymbol{k}}_b} \propto \frac{|\boldsymbol{k}_a|\,|\boldsymbol{k}_b|}{|\boldsymbol{k}_0/m_0 - \boldsymbol{k}_1/m_1|}\, \frac{1}{\boldsymbol{s}^4}\, |\psi_{mn}(\boldsymbol{q})|^2, \tag{8}$$

where m_0 and m_1 are the masses of the projectile electron and the lithium atom, respectively. The first factor on the right-hand side takes account of the incoming and outgoing fluxes of the impact ionization. Because of the indistinguishability between the scattered and ejected electrons, antisymmetrization of the electronic wave function leads to an exchange of the roles of $\boldsymbol{k}_a$ and $\boldsymbol{k}_b$ and a modification of the kinetic factor $1/\boldsymbol{s}^4$ of Eq. (8), which is given in Ref. [26]. Finally, since the spins of the incident and target electrons are usually unpolarized and the spins of the scattered and ejected electrons are not measured, the triply differential cross section must be averaged over initial spins and summed over final spins. For high-energy collisions, these spin-exchange effects on the dynamics of the ionization process are minimal; only the kinematic factors are altered.

As shown in Eq. (8), under the above approximations the triply differential cross section is proportional to the momentum density, $|\psi_{mn}(\boldsymbol{q})|^2$, of the orbital from which the electron is ejected. By selecting $\boldsymbol{k}_a$ and $\boldsymbol{k}_b$, and hence $\boldsymbol{q}$, one is able to map the momentum distribution of the valence orbital from the triply differential cross section. The symmetric noncoplanar configuration (Fig. 1) provides a convenient scheme for EMS because the momentum transfer $\boldsymbol{s}$ is independent of the azimuthal scattering angle φ; moreover, the kinetic factors [i.e., the first and the second factors in Eq. (8)] remain insensitive to small changes of φ near zero degrees even after antisymmetrization (see Fig. 3 of Ref. [28]). Therefore, the triply differential cross section as a function of φ can be directly interpreted as the momentum distribution of the ejected electron without further manipulation of the experimental data. The scattering angle θ can be chosen such that $q_y = 0$; thus

the momentum density along the z axis, $|\psi_{mn}(q_z)|^2$, can be imaged by rotating the azimuthal angles φ of both detectors. The z component of the momentum of the ejected electron at the instant of collision is determined by

$$q_z = 2k_f \sin\theta \, \sin\varphi, \tag{9}$$

where k_f is the momentum of each of the two outgoing electrons.

B. Time-resolved electron momentum spectroscopy

If target electronic states are nonstationary states, the above theory needs to be generalized to take account of the electronic motion. Time-dependent EMS theory has been developed for nonstationary states that can be represented as coherent superpositions of the eigenstates of the target [46]. However, in the case of laser-driven population transfer in lithium atoms, the scattering system is influenced by the external laser electromagnetic field, and hence the lithium target electronic state cannot be described simply as a coherent superposition state. In our previous works [47,54], we have developed a time-dependent distorted-wave approximation to simulate the diffraction of ultrafast electrons from laser-driven scattering target systems. This approximation fully accounts for the interaction between the laser and the scattering target system (in the electric dipole approximation) such that the dressing of the wave function of the incident electron and the population transfer in the lithium atoms can be accurately described, while the target-projectile interaction is modeled as a perturbation. This same idea is applicable to the current study. Since we have presented a detailed theoretical derivation and analysis in Ref. [54], we emphasize here the changes and additional approximations that are necessary to generalize the conventional EMS theory to the time-dependent case.

The first needed modification is to generalize the transition amplitude T_{mn} for the case of a system having a time-dependent Hamiltonian [54–56]. Since the Born approximation remains valid, the effects of the projectile-target interaction on the entrance wave function can be neglected. Then one can show, using the time-dependent distorted-wave approximation, that the transition amplitude from an initial state $\psi_i(t)$ to a final state $\psi_f(t)$ can be approximated by [cf. Eq. (2)]

$$\mathcal{T}_{fi} \simeq \int dt \big(\psi_f^{(-)}(t), V\, \psi_i^{(+)}(t)\big), \tag{10}$$

where $\psi_i^{(+)}(t)$ is the exact wave function of the entrance channel in the laser field satisfying the initial condition:

$$\psi_i^{(+)}(t) \to \psi_i(t) \quad \text{as } t \to -\infty. \tag{11}$$

Similarly, $\psi_f^{(-)}(t)$ is the wave function of the exit channel satisfying the asymptotic condition:

$$\psi_f^{(-)}(t) \to \psi_f(t) \quad \text{as } t \to \infty. \tag{12}$$

Thus $\psi_i^{(+)}(t)$ and $\psi_f^{(-)}(t)$ are the time-dependent counterparts (in the presence of the laser field) of the entrance and exit states appearing in Eq. (2), and Eq. (10) is the Born approximation counterpart of Eq. (2).

Before formulating expressions for $\psi_i^{(+)}(t)$ and $\psi_f^{(-)}(t)$ and evaluating the transition amplitude (10) for the population transfer, let us estimate the effects of the laser pulse on these wave functions. In laser-assisted impact ionization, if the projectile electron and/or the ejected electron absorb or emit photons, then the transition amplitude (10) comprises a sum of terms with each proportional to $J_l(\boldsymbol{q}\cdot\boldsymbol{\alpha})$, where J_l is the lth order Bessel function of the first kind, l indicates the number of absorbed or emitted photons, and $\boldsymbol{\alpha}$ is the displacement amplitude of an electron in the laser field [45,56,57]. In our simulations $|\boldsymbol{\alpha}| \lesssim 0.005$ a.u., since the laser field used to drive the population transfer in the lithium atom is assumed to have low intensity; see Sec. III for the laser parameters used in our simulations. Also, our interest is in valence electron momenta $|\boldsymbol{q}| \lesssim 1.5$ a.u. Thus the magnitudes of the arguments of the Bessel functions are much smaller than unity, so the probability that the electrons absorb or emit photons is negligible. In other words, the dressing of the incident and ejected electrons can be neglected and the only effect of the laser pulse is to drive the electronic motion in the lithium atom. Accordingly, instead of a Volkov wave, a plane wave is used to represent the incident high-energy electron in $\psi_i^{(+)}(t)$.

Time-dependent EMS theory requires a second modification of the representation of $\psi_i^{(+)}(t)$. In time-independent EMS theory (Sec. II A), the entrance state of the projectile electron and that of the lithium atom are assumed to be represented by single momentum states (or by an incoherent sum of momentum states), with each represented by a plane wave. However, in order to properly describe time-dependent scattering, localization of the incident electron and the lithium atom in both space and time is necessary in order to define the time of collision. This localization of the incident electron and the target can be accomplished using wave-packet integrals [22,46,58] that superpose plane-wave states χ_0 and χ_1 [cf. Eq. (3)]:

$$\psi_i^{(+)}(t) \simeq \int d\boldsymbol{k}_0\, d\boldsymbol{k}_1\, a_0(\boldsymbol{k}_0)\, a_1(\boldsymbol{k}_1)\, \chi_0(t)\, \chi_1(t)\, \psi_1(t). \tag{13}$$

Here $a_0(\boldsymbol{k}_0)$ and $a_1(\boldsymbol{k}_1)$ are the respective momentum amplitudes of the projectile electron and the lithium atom and $\psi_1(t)$ is the electronic wave function of the lithium atom. Note that these entrance states are generalized from the time-independent ones in Eq. (3) to time-dependent ones in accord with the first modification above. As shown later, the longitudinal extent (or longitudinal coherence) of the entrance states introduced by the wave-packet integrals is related to the temporal resolution of time-resolved EMS.

The electronic wave function $\psi_1(t)$ of the lithium atom target can be expanded in its field-free eigenstates ϕ_n. Since the lithium atom undergoes the laser-driven population transfer, $\psi_1(t)$ is different at each pump-probe delay time. In order to model this dependence on delay time, we assume that the population transfer is initiated prior to the collision by a time t_d, and, thus, $\psi_1(t)$ is displaced in time accordingly. Hence the wave packet of the projectile electron is the same for all delay times, but $\psi_1(t)$ at a given delay time t_d is

$$\psi_1(t) = \sum_n C_n(t + t_d)\, \phi_n\, e^{-i\omega_n(t+t_d)}, \tag{14}$$

where ω_n is the energy of the eigenstate ϕ_n and $C_n(t)$ is the amplitude at $t_d = 0$. The magnitude of $C_n(t)$ indicates the time-varying population of the ϕ_n state.

Similar considerations may be adduced for the exit-channel wave function, $\psi_f^{(-)}(t)$. Specifically, laser dressing of the states of the scattered electron, the ionized electron, and the lithium ion remains negligible, as are the distortions of the wave functions for these three particles. In other words, the validity of the plane-wave approximation for the final states is unaffected by generalizing the time-independent EMS theory to the time-dependent case. Therefore, the outgoing waves are approximated by

$$\psi_f^{(-)}(t) \simeq \chi_a(t)\,\chi_b(t)\,\chi_c(t)\,\phi_m^{-1}(t), \tag{15}$$

where $\chi_j(t)$ is the plane wave for the jth particle, $j \in \{a,b,c\}$ [see Eq. (1)].

Substituting Eqs. (13), (14), and (15) into Eq. (10), one obtains the following expression for the transition amplitude:

$$\mathscr{T}_{fi} \simeq \int d\boldsymbol{k}_0\, d\boldsymbol{k}_1\, a_0(\boldsymbol{k}_0)\, a_1(\boldsymbol{k}_1) \int dt\, e^{i(\varepsilon_f-\varepsilon_i)t} \times \sum_n C_n(t+t_d)\, T_{mn}\, e^{-i\omega_n t_d}. \tag{16}$$

Here ε_f and ε_i are respectively the total kinetic energies of the products and reactants and T_{mn} is evaluated using the plane-wave approximation [see Eq. (6)]. As shown in Eq. (16), the transition amplitude $\mathscr{T}_{fi}$ is a coherent superposition of the transitions T_{mn} weighted by the amplitudes of the wave packets and phases at the delay time t_d. If one further assumes the frozen-core approximation for T_{mn} [see Eq. (7) and the text below it], then the second line of Eq. (16) is proportional to $\sum_n C_n(t)\,\psi_{mn}(\boldsymbol{q})\,e^{-i\omega_n t}$ at the delay time t_d, which is the time-dependent, momentum-space wave function of the ejected electron.

The probability of the $(e,2e)$ process is defined by

$$\mathscr{P} = \int d\boldsymbol{k}_a\, d\boldsymbol{k}_b\, d\boldsymbol{k}_c\, |\mathscr{T}_{fi}|^2, \tag{17}$$

where the ranges of the final-momentum integrals depend on the experimental configuration. In typical EMS measurements, the momenta of the scattered and ejected electrons are measured, but the recoil momentum of the residual ion is not. Thus the ranges of $\boldsymbol{k}_a$ and $\boldsymbol{k}_b$ integrals are set by the energy and angular windows of the detectors and the momentum $\boldsymbol{k}_c$ is integrated over. As in conventional EMS theory [26], one must antisymmetrize the electronic wave function and, if the electrons are unpolarized, sum over the final spin states and average over the initial spin states. Furthermore, since the impact parameter $\boldsymbol{b}$ is rarely controlled with atomic precision in gas-phase collisions, an average of $\mathscr{P}$ over the relative positions between the projectile electrons and the lithium atoms in a gas ensemble is necessary. Therefore, the measured ensemble-averaged EMS probability is

$$\langle\mathscr{P}\rangle = \frac{1}{4}\sum_{s_a,s_b}\int d\boldsymbol{b}\,\rho(\boldsymbol{b})\,\mathscr{P}(s_a,s_b), \tag{18}$$

where $\rho(\boldsymbol{b})$ is the projected area density (along the propagation direction of the incident electrons) of the lithium atom gas, s_a and s_b denote the respective spins of the scattered and ejected electrons, and $\mathscr{P}(s_a,s_b)$ includes all possible spin configurations of the entrance channels.

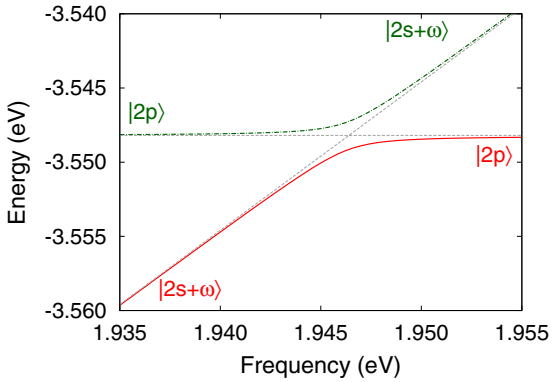

FIG. 2. Diabatic and adiabatic energy levels for the one-photon dressed $2s$ and $2p$ states of lithium atoms as a function of the laser frequency. The diabatic energies for the one-photon dressed $2s$ and $2p$ states are represented by the diagonal and horizontal dashed lines, respectively. The solid (red) and dash-dotted (green) lines are the adiabatic energies that connect the dressed $2s$ and $2p$ states. The amplitude of the laser electric field is 3.00×10^{-5} a.u., corresponding to an intensity of 3.16×10^7 W/cm^2. The frequency of the laser is given in units of eV.

C. Frequency-swept adiabatic passage

The frequency-swept adiabatic passage technique [59,60] is chosen to perform the population transfer in lithium atoms owing to its simplicity and controllability. This scheme can be understood within a dressed-state picture. Figure 2 shows the photon-dressed energy diagram of the lowest two electronic states of the lithium atom as a function of laser frequency. The diagonal and the horizontal dashed lines are the diabatic energies of the one-photon dressed $2s$ and the $2p$ states, respectively. (Since the population transfer is essentially a one-electron process, the eigenstates ϕ_n of the valence electron are labeled by their orbitals.) The energy of the dressed $2s$ state increases linearly with laser frequency and the two diabatic energies cross at the $2s$-$2p$ resonance frequency. On the other hand, the adiabatic energies (indicated by the solid and dash-dotted lines) have an avoided crossing near the resonant frequency that connects the dressed $2s$ and $2p$ states. Therefore, if the population transfer starts from a negative detuning and the instantaneous frequency of the laser pulse is swept upward adiabatically, then the population of the lithium atoms follows the lower adiabatic level and is transferred to the $2p$ state.

III. SIMULATION DETAILS

As many details of our simulations have been discussed in the context of ultrafast electron diffraction [47,54], we focus on those aspects that are unique to the $(e,2e)$ process and only summarize briefly our numerical procedures. Since the lithium electronic state $\psi_1(t)$ is written in terms of its eigenstates [see Eq. (14)], the first step is to calculate ϕ_n. An independent particle representation is employed, so that ϕ_n is constructed from a Slater determinant of single-particle orbitals. These orbitals are calculated using the Herman-Skillman potential [61], which is obtained by solving the Hartree-Fock equation within a central-field approximation in which the electron-electron

interaction is replaced by the Hartree-Fock-Slater potential. We neglect fine-structure effects. While the Herman-Skillman potential is unable to provide spectroscopic accuracy, it serves well for our current purpose of demonstrating the capability of EMS to image electronic motions and it allows us to identify the features of those electronic motions that are reflected in the time-resolved spectra.

After obtaining the eigenstates, the second step is to simulate the laser-driven population transfer process in the lithium atom targets. The time-dependent Schrödinger equation is solved numerically, from which the amplitude $C_n(t)$ of each eigenstate [see Eq. (14)] can be obtained. We use a linearly polarized laser electric-field pulse having a Gaussian envelope and a full width at half maximum (FWHM) duration of 2.0 ps. The peak intensity of the pulse is 1.93×10^7 W/cm^2. The chirp is 1.5×10^{-3} eV/ps, and the instantaneous frequency equals the $2s$-$2p$ resonant frequency (1.946 eV) at the peak of the laser pulse. These laser parameters are chosen such that the time scale of the population transfer is controlled to be of the order of a few ps, which is longer than the fs electron pulses but shorter than the lifetime of the excited $2p$ state. The valence electron in the initial state of the lithium atom is in the $2s$ state. We neglect multiphoton ionization during the population transfer.

The time-resolved EMS spectra are calculated according to Eq. (18). The incident electron pulses have a central kinetic energy of 5.0 keV, so the first-order Born approximation should be adequate to describe impact ionization near the Bethe ridge [62]. The momentum density $|a_0(\boldsymbol{k}_0)|^2$ is described by a Gaussian distribution whose width along the longitudinal direction is set by the incident electron pulse duration. Two pulse durations are considered in our simulations: 100 fs and 1 fs (FWHM). We also assume the pulses are transform limited (i.e., chirpless), so that the corresponding bandwidths are 0.018 and 1.8 eV (FWHM). The width of $a_0(\boldsymbol{k}_0)$ in the transverse direction is set by the angular divergence of the incident electron beam. However, since the polar angles of the scattered and ejected electrons are $\theta \approx 45^\circ$ in the symmetric nonplanar configuration, as long as the angular divergence does not affect the momentum resolution, the small angular divergence of a well-collimated pulse is not significant. Therefore, the transverse spread of $a_0(\boldsymbol{k}_0)$ is neglected.

The calculation of T_{mn} requires the momentum wave functions of the lithium atom [see Eqs. (6) and (7)], which are computed by calculating the Fourier transforms of the Hartree-Slater $2s$ and $2p$ eigenstates for the valence electron. Since the central-field approximation is used to calculate the orbitals of the lithium atom, the orbital wave functions factorize into radial and angular parts. Accordingly, the Fourier transform factors into two parts: the radial part is calculated numerically and the angular part is simply a spherical harmonic.

We assume the ensemble of lithium atoms has a homogeneous transverse distribution whose dimension is much larger than the cross section of the incident electron pulses. The longitudinal width of the ensemble is assumed to be 50 μm in order to reduce the effect of group-velocity mismatch between the laser pump and electron probe pulses. The density of the lithium atom ensemble is assumed to be 10^{10} cm^{-3} [63], so that the projected area density of the lithium atom gas is $\rho(\boldsymbol{b}) = 5.0 \times 10^7$ cm^{-2}.

The energy and angular windows of the detectors are assumed to be rectangle functions centered at the corresponding nominal values. The width of the energy window is 0.6 eV and the widths $\Delta\theta$ and $\Delta\varphi$ of the angular windows for different simulations are specified when presenting the results in Sec. IV. The final-momentum integrals are performed using Gaussian quadrature. As in time-independent EMS theory, the scattering angle θ can be chosen such that $q_y = 0$ (where $\boldsymbol{q} \equiv \boldsymbol{k}_a + \boldsymbol{k}_b - \boldsymbol{k}_0$); it must be varied according to the energies of the two outgoing electrons. Then, the momentum density along the z axis, $|\psi_{mn}(q_z)|^2$ [see Eq. (7)], can be obtained by varying the azimuthal angles φ of both detectors [see Eq. (9)].

IV. RESULTS AND DISCUSSION

In this section we briefly summarize our results for the laser-driven $2s \rightarrow 2p$ population transfer process in the target Li atoms and then present our EMS results for incident electron pulses having durations of 100 fs and 1 fs.

Before beginning the presentation of our results, however, we remark upon the terminology used in this work. Since nonstationary states superpose eigenstates with different energies [see Eq. (14)] and since multiple momentum components are included in the incident electron wave packet [see Eq. (13)], in general one may not use the conservation of energy in the time-dependent EMS case to identify the ionization transitions from EMS measurements. In other words, the ensemble-averaged probabilities $\langle \mathscr{P} \rangle$ (18), unlike the differential cross sections in conventional EMS [see Eq. (8)], are not necessarily associated with the momentum density of a single orbital, even with perfect detector resolution. In particular, as we will show, $\langle \mathscr{P} \rangle$ can depend on the properties of incident electron pulses (e.g., their bandwidth). Therefore, in this work we define the *EMS spectrum* as the ensemble-averaged probability $\langle \mathscr{P} \rangle$, which is a function of (i) the energy difference between the incident electron energy and the energies of the two outgoing electrons and (ii) the azimuthal angle φ of the detectors. Also, the EMS spectra at *fixed energies* are called *momentum profiles* (or simply profiles if there is no ambiguity) in order to distinguish them from the *momentum density* of the probed state, which is an intrinsic property independent of how the experimental measurements are carried out.

A. Li $2s \rightarrow 2p$ population transfer

Although the results of the $2s \rightarrow 2p$ population transfer in the Li atoms have been reported in Refs. [47,54], for the purpose of completeness we reproduce the main features of those results here. Figure 3 presents the populations of the electronic states of the Li atom as a function of time. Different lines correspond to different electronic states labeled according to the legends and the shaded area indicates the profile of the driving laser electric field. One sees that the time scale of the population transfer is about 3 ps, that the $2s$ population (solid line) decreases monotonically, and that the $2p$ population (dash-dotted line) grows monotonically. At the end of the process almost all the initial $2s$ population is transferred to the $2p, m_l = 0$ state; moreover, other excited states have negligible populations throughout the entire process.

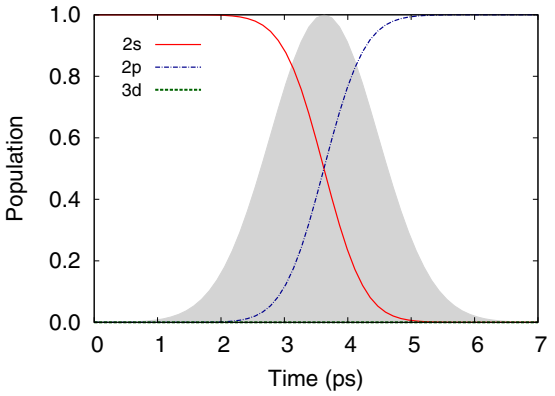

FIG. 3. Populations of the $2s$, $2p$, and $3d$ states of the lithium atom undergoing a laser-driven population transfer as a function of time. The shaded area indicates the envelope of the electric field of the pump laser.

B. EMS for 100 fs incident electron pulses

Time-resolved EMS spectra of the Li $2s \rightarrow 2p$ population transfer imaged by 5.0 keV 100 fs incident electron pulses at four different pump-probe delay times are shown in Fig. 4. The abscissa is the binding energy of the ejected electrons, defined as the energy difference between the central energy of the incident electron and the central energy of the pair of outgoing electrons and the ordinate is the azimuthal angle φ of the detectors (see Fig. 1). A positive angle φ corresponds to a positive z component of $\boldsymbol{q}$ [see Eq. (9)]. The delay time is defined with respect to the onset of population transfer (i.e., the time zero of Fig. 3), not the peak-to-peak time difference between the pump and probe pulses. The energy window of the detectors is 0.6 eV and the angular windows are $\Delta\theta \times \Delta\varphi = 0.5^\circ \times 0.5^\circ$. While the energy resolution of the spectrum results from the convolution of the bandwidth of the incident electron pulse, the energy distribution of the target electronic motion, and the energy resolution of the detector, for the 100 fs case the widths of the peaks in the spectrum stem mainly from the energy resolution of the detector.

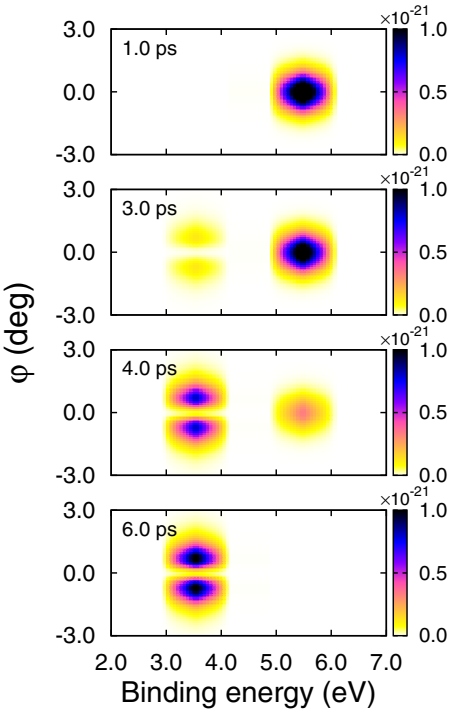

FIG. 4. Time-resolved EMS spectra of an electronic population transfer in target Li atoms imaged by 5.0 keV 100 fs (FWHM) incident electron pulses at four pump-probe delay times, $t_d = 1.0, 3.0, 4.0$, and 5.0 ps. The adiabatic $2s \rightarrow 2p$ population transfer in the Li atoms is driven by a chirped laser pulse (see Fig. 3). The delay times are measured from the time zero of the population transfer. The energy window of the detectors is 0.6 eV and the angular window is $\Delta\theta \times \Delta\varphi = 0.5^\circ \times 0.5^\circ$.

The spectra in Fig. 4 exhibit two separate distributions centered at binding energies of 3.6 and 5.5 eV and their intensities vary with the time delay t_d. The distributions at higher and lower binding energies correspond to ionization from the $2s$ and $2p$ orbitals, respectively. Although both distributions are symmetric with respect to $\varphi = 0^\circ$, they show distinct momentum profiles since the electron is ionized from orbitals having different symmetries. The $2s$ distribution peaks at $\varphi = 0^\circ$, but the $2p$ one has a minimum at $\varphi = 0^\circ$, which is consistent with the zero-momentum node of the $2p$ orbital. In addition to distinct momentum profiles, the two distributions show opposite temporal behaviors. Since the majority of the population remains in the $2s$ state at $t_d = 1.0$ ps (see Fig. 3), only the $2s$ distribution can been seen in the $t_d = 1$ ps spectrum. Then, as t_d increases, the $2s$ profile gradually disappears while the $2p$ profile emerges, thus reflecting the $2s \rightarrow 2p$ population transfer. Because of the spectroscopic measurements, the time-resolved spectra reflect the changes in the energy composition of the electronic motion during the population transfer. In short, these results demonstrate the capability of time-dependent EMS to differentiate and image the time-varying momentum density of the valence electron during the population transfer.

In order to compare quantitatively the measured momentum profiles with the momentum densities of the valence orbitals of the Li atom, we present in Fig. 5 the profiles of the $2s$ and $2p$ distributions from Fig. 4 and the momentum densities of the $2s$ and $2p$ orbitals. (Note that the results in Fig. 5 are presented on a logarithmic scale, whereas those in Fig. 4 are presented on a linear scale.) The energies of the momentum profiles of the $2s$ and $2p$ states are chosen at their corresponding binding energies (i.e., 5.5 and 3.6 eV, respectively); also, results are presented for $\varphi \geqslant 0$. Since the momentum resolution is highly dependent on the angular resolution of the detectors for the 100 fs case, in Fig. 5 we also compare the sensitivity of the momentum profiles to the angular resolution of the detectors by varying the angular windows $\Delta\theta$ and $\Delta\varphi$ for three different cases, as indicated by the legends in Fig. 5(b). In order to compare the shapes of the profiles for different detection windows, the profiles are rescaled such that the maxima of the profiles are normalized to unity.

As shown in Fig. 5(a), the node of the $2s$ orbital is well reproduced by the angular windows having $\Delta\varphi = 0.5^\circ$ (dotted and dashed lines), whereas the momentum profile for the angular window having $\Delta\varphi = 2.0^\circ$ (dash-dot-dot line) lacks a clear nodal structure and spans a wider range of φ than the $2s$ momentum density. For the $2p$ case, the profile for the angular window having $\Delta\varphi = 2.0^\circ$ also fails to reproduce the zero-

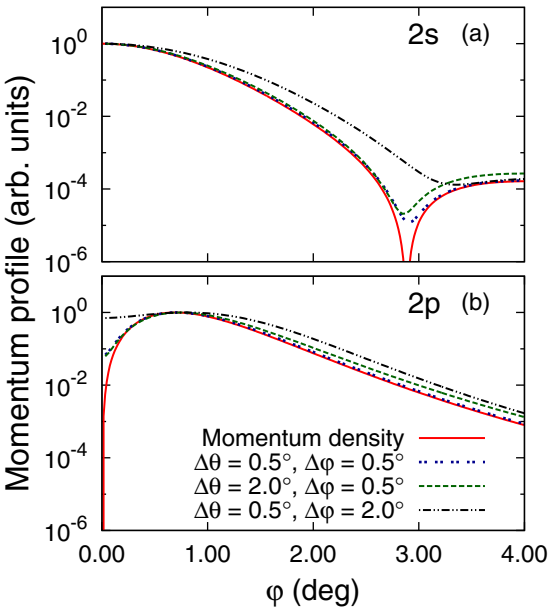

FIG. 5. Sensitivity of momentum profiles for the $2s$ (a) and the $2p$ (b) states to the angular resolution of the detector. The $2s$ and $2p$ profiles are presented from the results in Fig. 4 at their corresponding binding energies (5.5 and 3.6 eV) for time delays $t_d = 1.0$ ps and 6.0 ps, respectively, and for an energy window 0.6 eV. The red solid lines represent the momentum densities of the corresponding states and the profiles for three different angular windows of the detector are indicated in the legends of panel (b). See Fig. 1 for the definition of the angular window. For ease of comparison, the momentum profiles and densities are scaled such that their maxima are normalized to unity. Results are presented on a logarithmic scale.

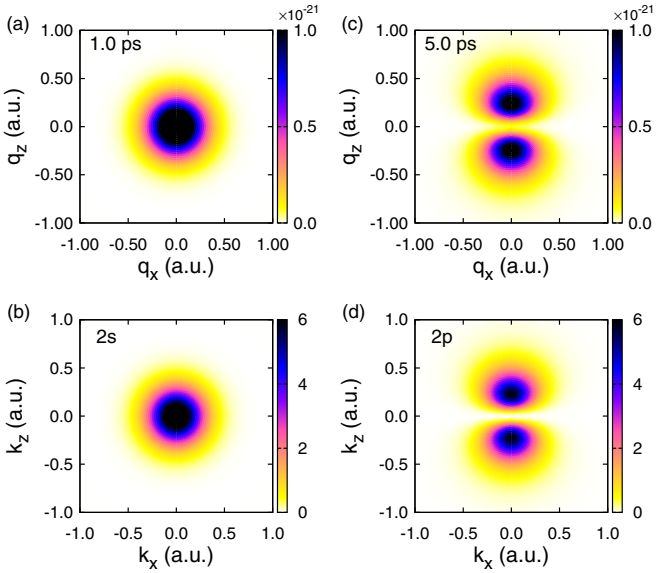

FIG. 6. Comparison of two-dimensional momentum profiles at time delays (a) $t_d = 1.0$ ps and (c) 5.0 ps (top row) with the corresponding momentum densities of (b) the $2s$ and (d) the $2p$ orbitals in the x-z plane (bottom row). Two-dimensional profiles are obtained by rotating the polarization of the pump laser. However, the profiles are presented in the coordinate frame of the Li atom in which the z axis is along the direction of the laser polarization. The energy window of the detector is 0.6 eV and the angular windows are $\Delta\theta \times \Delta\varphi = 0.5^\circ \times 0.5^\circ$. The momentum profiles are presented in terms of nominal momentum $\boldsymbol{q}$ calculated from the central momentum values of $\boldsymbol{k}_a$, $\boldsymbol{k}_b$, and $\boldsymbol{k}_0$ [see Eq. (9)].

momentum node. The profiles in both cases are more sensitive to $\Delta\varphi$ than to $\Delta\theta$ because (i) for high-energy incident electron pulses the momentum profiles are confined to a small range of φ around zero degrees and (ii) at small φ, the uncertainty in Δq_z is dominated by $\Delta\varphi$ [see Eq. (9)]. Thus, if the width of the angular window $\Delta\varphi$ approaches that of the range of φ over the momentum profile of the target state, then one quickly loses sufficient momentum resolution. For both the $2s$ and $2p$ orbitals the agreement between the momentum profiles for the case of the angular window $\Delta\theta \times \Delta\varphi = 2.0^\circ \times 0.5^\circ$ (dashed line) and the corresponding momentum densities decreases as φ increases, whereas for the case of the angular window $0.5^\circ \times 0.5^\circ$ (dotted line) the comparisons are quite good for all values of φ. This may be attributed to the asymmetric detection windows and the bigger effect of averaging over q_z for the uncertainty $\Delta\theta$ at larger values of φ.

In addition to the time dependence of the momentum profiles, a distinctive feature of time-resolved EMS for the case of photoinduced target reactions is the ability to image the anisotropy of the resulting electronic motions. Conventional EMS commonly measures unoriented targets, so only one-dimensional (spherically averaged) momentum profiles can be retrieved from the measurements. On the other hand, two- or three-dimensional momentum profiles can be obtained from polarized electronic motions, which provides information on the electrons' geometric motions (or on molecular steric transitions). Hence, if one varies the polarization axis of the laser pulse with respect to the z axis of the spectrometer, one obtains the momentum profiles of the $2s$ and $2p$ orbitals in the x-z plane [see Figs. 6(a) and 6(c)], which are compared with the corresponding momentum densities. The angular distributions and symmetries of the momentum profiles agree well with the two-dimensional momentum densities [see Figs. 6(b) and 6(d)]. However, since we neglect the dressing of the laser field on the incident and outgoing electrons in our model, in practice small p and s characters may be observed in the respective $2s$ and $2p$ profiles if the amplitudes for photon emission or absorption are appreciable.

C. EMS for 1 fs incident electron pulses

The EMS results for 100 fs incident electron pulses successfully differentiate the momentum densities of the Li $2s$ and $2p$ orbitals and the time-resolved spectra exhibit two separated distributions whose intensities reflect their populations at the moment of collision (Fig. 4). The conventional momentum-density interpretation (Sec. II A) thus seems extendable to time-resolved EMS. However, since there is only a *single* valence electron involved in the population transfer, the *two* disconnected distributions in the spectrum suggest that the valence electron of each Li atom jumps discontinuously between the two states. On the other hand, as shown in Figs. 2 and 3, the population transfer is a continuous process in which the wave function of the Li valence electron progressively evolves from the $2s$ state to the $2p$ state. The discontinuity suggests

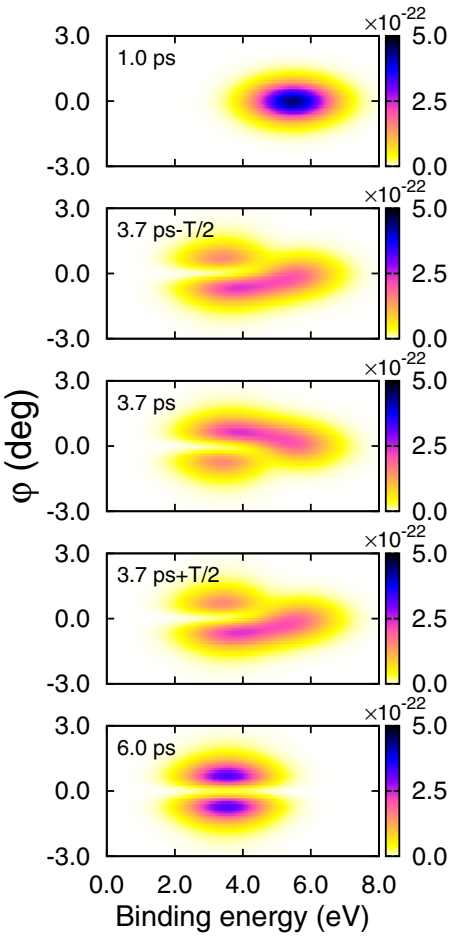

FIG. 7. Time-resolved EMS spectra of the time-varying electronic motion in Li atoms for 1 fs (FWHM) incident electron pulses at delays $t_d = 1.0, 3.7 - T/2, 3.7, 3.7 + T/2$, and 6.0 ps. The $2s$-$2p$ beat period is $T \approx 2.13$ fs. The energy window is 0.6 eV and the angular windows are $\Delta\theta \times \Delta\varphi = 0.5^\circ \times 0.5^\circ$.

some information on the electronic motion is missing from the 100 fs momentum profiles. By inspecting Eq. (14) one observes that, in addition to the slow laser-driven population transfer, the Li valence state oscillates rapidly owing to the quantum beat originating from the energy difference between the $2s$ and $2p$ states. Moreover, since the $2s$ and $2p$ states have opposite parities, the electron density wiggles from one side of the core to the other with a beat period of $T \approx 2.13$ fs. To resolve such electronic motion during the population transfer, we study here the use of 1 fs incident electron pulses to measure the momentum density.

The EMS results for 1 fs incident electron pulses are presented as a function of pump-probe delay time in Fig. 7. The middle three panels are for delay times that differ by half the beat period T (with the central one at 3.7 ps) in order to image the wiggling of the electronic motion. In contrast to the 100 fs case, the energy resolution is now dominated by the energy spread of the incident electron pulses.

Contrary to the 100 fs spectra (Fig. 4), the 1 fs spectra show a *single* distribution that evolves continuously from the $2s$ to $2p$ profiles as the delay time increases. At $t_d = 1.0$ and 6.0 ps, the spectra exhibit the respective $2s$ and $2p$ characters as observed in the 100 fs case (except that the distributions are wider in energy due to the larger bandwidth of the 1 fs electron pulses). However, as the population transfer progresses, one sees in the middle three panels only a single distribution spanning continuously across the energy region of the $2s$ and $2p$ binding energies. Moreover, these spectra are not simply a superposition of the $2s$ and $2p$ profiles weighted by their populations as observed in the 100 fs case, but they show an energy- and φ-dependent structure. The high- and low-energy sides of each distribution exhibit respectively the $2s$- and $2p$-like profiles, while in the middle energy region (≈4.0 eV) one sees an *asymmetric* distribution with respect to $\varphi = 0^\circ$. The spectrum also shows rapid oscillation as the delay time changes and the similarity between the second and fourth panels indicates that the period of the oscillation conforms with the $2s$-$2p$ beat period. These distinctive features are a reflection of the details of the electronic motion during the population transfer.

Although a deeper layer of information on the electronic motion is revealed by the 1 fs incident electron pulses, the intuitive interpretation of EMS spectra cannot be directly applied to the 1 fs spectra. For the 100 fs case, the momentum profile of an orbital can be determined by its binding energy, provided one has adequate energy resolution and no degeneracy. For the 1 fs case, the momentum profiles at the valence orbital binding energies do not indicate the momentum density of the valence electron. Since only the pulse duration is changed in the two simulations, the energy-dependent structure results from the interplay between the energy distributions of the incident electron and the Li atom's valence electron. One may ask whether the 1 fs spectrum still possesses a momentum-density interpretation even though the energy resolution is reduced by the pulse bandwidth.

In order to investigate this, in Fig. 8 we compare the momentum density with the two-dimensional momentum profiles from the EMS spectra of the 1 fs pulses as a function of the time delay t_d for three binding energies: those of the $2s$ and $2p$ states as well as one between them (4.4 eV). We have chosen five time delays beginning at $t_{\rm ref} = 3.6992$ ps and increasing by intervals of $T/8$, so that the results in Fig. 8 extend over half the beat period. The momentum density in the right-hand column of Fig. 8 shows asymmetric distributions: the wiggling motion begins with a negatively skewed momentum distribution (i.e., $k_z < 0$) along the z axis (corresponding to downward spatial motion) that reverses its direction of motion at the end of the time delay series (corresponding to upward spatial motion). Of the three momentum profiles (first three columns in Fig. 8), the profile for the energy 4.4 eV agrees best with the momentum density.

One can understand this agreement by analyzing the time-dependent transition amplitude (16). According to the EMS conditions discussed in Sec. II A, each ionization transition from an initial state ϕ_n to an ionic state ϕ_m^{-1} is associated with a peak in the EMS spectrum, whose position depends on the energy exchanged between the projectile electron and the (ionized) valence electron. The spectral line shape results from the convolution of the line shape of the valence electron state and the energy distribution of the incident electron. (To simplify the discussion, no effects of the energy resolution of the detectors are considered here.) If the valence electron state is a nonstationary state, the transition amplitude $\mathcal{T}_{fi}$ is a superposition of the constituent transitions T_{mn}, each of which

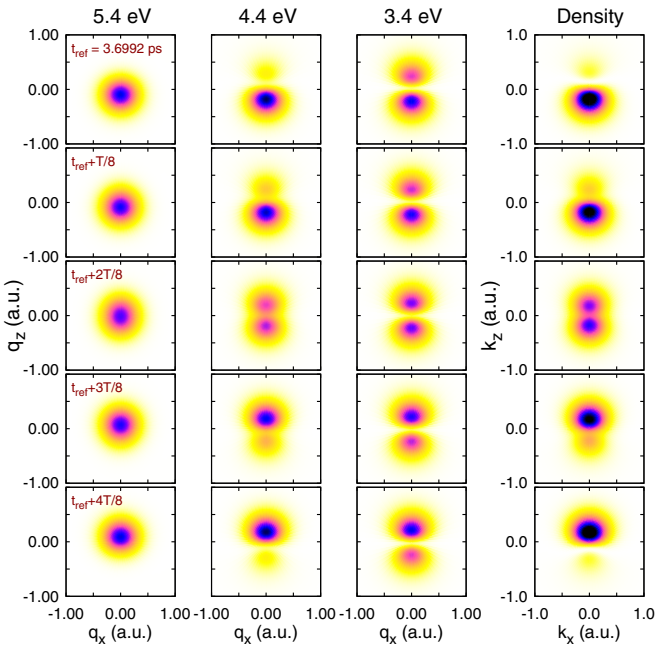

FIG. 8. Sequence of two-dimensional momentum profiles and densities of the wiggling valence electron motion in Li at delay times spanning half of the $2s$-$2p$ beat period in the x-z plane. The pump-probe delay times are given in the panels of the first column. The left three columns show the momentum profiles at three binding energies (3.4, 4.4, and 5.4 eV) labeled at the top and the rightmost column shows the corresponding momentum densities.

corresponds to a different energy exchange. Thus the scattered wave comprises different energy components. If the bandwidth of the incident electron pulse is narrower than the energy differences of the $2s$ and $2p$ valence electron states, the various components of the scattered wave are well separated in energy and multiple peaks appear in the spectrum, as seen in the 100 fs case (Fig. 4). On the other hand, as the duration of the incident electron pulse decreases, adjacent peaks in the spectrum begin to overlap. Moreover, each component of the scattered wave carries phase information of the target electronic motion at the moment of collision (as well as phase information on the incident electron). Therefore, the overlap of the various scattered wave components results in an interference in the spectrum that is observed at energies between two adjacent transitions. This is the reason we observe a single, continuous distribution in the 1 fs spectra (Fig. 7) and the momentum profile midway between the two valence states (i.e., at 4.4 eV) gives the most accurate momentum profile (Fig. 8).

D. Discussion of the 100 fs and 1 fs results

Our results for incident electron pulses having 100 fs and 1 fs durations illustrate how the pulse duration controls the kinds of information one can extract from time-dependent EMS spectra. If the pulse duration is short enough (i.e., has adequate coherent bandwidth) and still has good monochromaticity (i.e., the central energy is much larger than the bandwidth), then the ensemble-averaged probability is insensitive to details of the electron pulse and is proportional to the momentum density of the ejected electron at the time t_d [22,46,58]:

$$\langle \mathscr{P} \rangle \propto \left| \sum_n C_n(t_d)\, \psi_{mn}(\boldsymbol{q})\, e^{-i\omega_n t_d} \right|^2. \tag{19}$$

On the other hand, if duration of the incident electron pulse is much longer than the $2s$-$2p$ beat period (but still short enough to resolve the population transfer), then the valence electron oscillates many times during the collision. Therefore, the phase information is lost and the probability is proportional to the momentum density of the orbital weighted by its population at the corresponding binding energy:

$$\langle \mathscr{P} \rangle \propto \sum_n |C_n(t_d)|^2\, |\psi_{mn}(\boldsymbol{q})|^2. \tag{20}$$

V. SUMMARY AND CONCLUSION

To summarize, we have presented a time-dependent theory for EMS of the Li valence electronic state that undergoes a laser-driven population transfer. This electronic motion consists of a slow $2s \rightarrow 2p$ population transfer on a ps time scale and a rapid wiggling of the electron density on a fs time scale. Simulations of the 100 fs and 1 fs electron pulses demonstrate the capability of EMS to resolve and differentiate the time-varying momentum density and the associated change of symmetry of the electronic motion.

The information about the electronic motion and the interpretation of the time-resolved EMS spectra depends on the pulse duration relative to the time scale of the electronic motion. For the 100 fs case, the EMS spectra can be understood using the conventional momentum-density interpretation. The spectra show the momentum profiles of the orbitals participating in the population transfer and the intensities of the profiles reflect the time-dependent populations of the corresponding orbitals. For the 1 fs case, the EMS can differentiate the relative phases between the eigenstates participating in the population transfer, so a complete picture of the electronic motion can be observed in the spectra. The momentum profiles show asymmetric distributions with respect to the x-y plane, reflecting the wiggling motion of the valence electron as a result of quantum beating. The momentum-density interpretation can still be directly applied to the 1 fs case by properly selecting the momentum profiles from the EMS spectra.

Although the EMS spectra of an atomic system lack some features observed for molecular targets, it nevertheless provides a simple, controllable, and comprehensible system for advancing time-resolved EMS measurements and provides a basis for understanding the electron dynamics involved in molecular reactions. Unlike traditional spectroscopic measurements, the interpretation of the EMS spectra is straightforward and unequivocal and the retrieved information of the target electronic motions is unique. Moreover, as shown in the present simulations, the EMS spectra for a laser-driven target electronic motion exhibit features that are sensitive to the incident electron pulse duration. Therefore, such a system can serve as a prototype for investigating time-resolved measurements of EMS and for examining the assumptions of the present theoretical model. Although EMS suffers from low statistics and presents many experimental challenges, owing to its advantages, it seems worthwhile to pursue time-resolved EMS further.

ACKNOWLEDGMENTS

This work was supported by the US National Science Foundation under Grant No. PHYS-1505492. This work was completed utilizing the Holland Computing Center of the University of Nebraska, which receives support from the Nebraska Research Initiative.

[1] P. Wernet, Electronic structure in real time: Mapping valence electron rearrangements during chemical reactions, Phys. Chem. Chem. Phys. **13**, 16941 (2011).
[2] T. Jahnke, Interatomic and intermolecular Coulombic decay: The coming of age story, J. Phys. B **48**, 082001 (2015).
[3] R. Pazourek, S. Nagele, and J. Burgdörfer, Attosecond chronoscopy of photoemission, Rev. Mod. Phys. **87**, 765 (2015).
[4] K. Ramasesha, S. R. Leone, and D. M. Neumark, Real-time probing of electron dynamics using attosecond time-resolved spectroscopy, Annu. Rev. Phys. Chem. **67**, 41 (2016).
[5] M. Nisoli, P. Decleva, F. Calegari, A. Palacios, and F. Martín, Attosecond electron dynamics in molecules, Chem. Rev. **117**, 10760 (2017).
[6] M. Th. Hassan, J. S. Baskin, B. Liao, and A. H. Zewail, High-temporal-resolution electron microscopy for imaging ultrafast electron dynamics, Nat. Photon. **11**, 425 (2017).
[7] K.-J. Yuan and A. D. Bandrauk, Exploring coherent electron excitation and migration dynamics by electron diffraction with ultrashort x-ray pulses, Phys. Chem. Chem. Phys. **19**, 25846 (2017).
[8] F. Krausz and M. Ivanov, Attosecond physics, Rev. Mod. Phys. **81**, 163 (2009).
[9] M. Chini, K. Zhao, and Z. Chang, The generation, characterization, and applications of broadband isolated attosecond pulses, Nat. Photon. **8**, 178 (2014).
[10] S. Corde, K. Ta Phuoc, G. Lambert, R. Fitour, V. Malka, A. Rousse, A. Beck, and E. Lefebvre, Femtosecond x rays from laser-plasma accelerators, Rev. Mod. Phys. **85**, 1 (2013).
[11] C. Bostedt, S. Boutet, D. M. Fritz, Z. Huang, H. J. Lee, H. T. Lemke, A. Robert, W. F. Schlotter, J. J. Turner, and G. J. Williams, Linac coherent light source: The first five years, Rev. Mod. Phys. **88**, 015007 (2016).
[12] G. Sciaini and R. J. D. Miller, Femtosecond electron diffraction: Heralding the era of atomically resolved dynamics, Rep. Prog. Phys. **74**, 096101 (2011).
[13] C. Kealhofer, W. Schneider, D. Ehberger, A. Ryabov, F. Krausz, and P. Baum, All-optical control and metrology of electron pulses, Science **352**, 429 (2016).
[14] E. Goulilmakis *et al.*, Real-time observation of valence electron motion, Nature (London) **466**, 739 (2010).
[15] F. Zamponi, P. Rothhardt, J. Stingl, M. Woerner, and T. Elsaesser, Ultrafast large-amplitude relocation of electronic charge in ionic crystals, Proc. Natl. Acad. Sci. USA **109**, 5207 (2012).
[16] D. M. Villeneuve, P. Hockett, M. J. J. Vrakking, and H. Niikura, Coherent imaging of an attosecond electron wave packet, Science **356**, 1150 (2017).
[17] A. R. Beck, D. M. Neumark, and S. R. Leone, Probing ultrafast dynamics with attosecond transient absorption, Chem. Phys. Lett. **624**, 119 (2015).
[18] M. Wu, S. Chen, S. Camp, K. J. Schafer, and M. B. Gaarde, Theory of strong-field attosecond transient absorption, J. Phys. B **49**, 062003 (2016).
[19] S. P. Neville, V. Averbukh, S. Patchkovskii, M. Ruberti, R. Yun, M. Chergui. A. Stolow, and M. S. Schuurman, Beyond structure: Ultrafast x-ray absorption spectroscopy as a probe of non-adiabatic wavepacket dynamics, Faraday Discuss. **194**, 117 (2016).
[20] K. Kunnus *et al.*, Anti-Stokes resonant x-ray Raman scattering for atom specific and excited state selective dynamics, New J. Phys. **18**, 103011 (2016).
[21] G. Dixit, O. Vendrell, and R. Santra, Imaging electronic quantum motion with light, Proc. Natl. Acad. Sci. USA **109**, 11636 (2012).
[22] H.-C. Shao and A. F. Starace, Imaging coherent electronic motion in atoms by ultrafast electron diffraction, Phys. Rev. A **88**, 062711 (2013).
[23] V. S. Yakovlev, M. I. Stockman, F. Krausz, and P. Baum, Atomic-scale diffractive imaging of sub-cycle electron dynamics in condensed matter, Sci. Rep. **5**, 14581 (2015).
[24] I. E. McCarthy and E. Weigold, Electron momentum spectroscopy of atoms and molecules, Rep. Prog. Phys. **54**, 789 (1991).
[25] M. A. Coplan, J. H. Moore, and J. P. Doering, (e,2e) spectroscopy, Rev. Mod. Phys. **66**, 985 (1994).
[26] E. Weigold and I. E. McCarthy, *Electron Momentum Spectroscopy* (Kluwer Academic/Plenum Publishers, New York, 1999).
[27] C. E. Brion, G. Cooper, Y. Zheng, I. V. Litvinyuk, and I. E. McCarthy, Imaging of orbital electron densities by electron momentum spectroscopy – a chemical interpretation of the binary (e,2e) reaction, Chem. Phys. **270**, 13 (2001).
[28] M. Takahashi, Looking at molecular orbitals in three-dimensional form: From dream to reality, Bull. Chem. Soc. Jpn. **82**, 751 (2009).
[29] M. Inokuti, Inelastic collisions of fast charged particles with atoms and molecules – The Bethe theory revisited, Rev. Mod. Phys. **43**, 297 (1971).
[30] R. Camilloni, A. G. Guidoni, I. E. McCarthy, and G. Stefani, Mechanism of the (e,2e) reaction with atoms, Phys. Rev. A **17**, 1634 (1978).
[31] E. Weigold, C. J. Noble, S. T. Hood, and I. Fuss, Electron impact ionisation of atomic hydrogen: Experimental and theoretical (e,2e) differential cross sections, J. Phys. B **12**, 291 (1979).
[32] J. P. D. Cook, I. E. McCarthy, J. Mitroy, and E. Weigold, Electron momentum spectroscopy of xenon: A detailed analysis, Phys. Rev. A **33**, 211 (1986).
[33] B. Lohmann and E. Weigold, Direct measurement of the electron momentum probability distribution in atomic hydrogen, Phys. Lett. A **86**, 139 (1981).
[34] G. Stefani and R. Camilloni, Impulsive (e,2e) energy-sharing experiments on He, J. Phys. B **18**, 499 (1985).
[35] C. G. Ning, B. Hajgató, Y. R. Huang, S. F. Zhang, K. Liu, Z. H. Luo, S. Knippenberg, J. K. Deng, and M. S. Deleuze,

High resolution electron momentum spectroscopy of the valence orbitals of water, Chem. Phys. **343**, 19 (2008).

[36] Y. R. Miao, J. M. Li, J. K. Deng, and C. G. Ning, High resolution $(e,2e)$ spectroscopy of dimethyl ether, J. Electron Spectrosc. Relat. Phenom. **193**, 1 (2014).

[37] C. G. Ning, Z. H. Luo, Y. R. Huang, B. Hajgató, F. Morini, K. Liu, S. F. Zhang, J. K. Deng, and M. S. Deleuze, Investigation of the molecular conformations of ethanol using electron momentum spectroscopy, J. Phys. B **41**, 175103 (2008).

[38] S. H. R. Shojaei, F. Morini, and M. S. Deleuze, Photoelectron and electron momentum spectroscopy of tetrahydrofuran from a molecular dynamical perspective, J. Phys. Chem. A **117**, 1918 (2013).

[39] M. Yamazaki, H. Satoh, N. Watanabe, D. B. Jones, and M. Takahashi, Oscillation of the electron-density distribution in momentum space: An $(e,2e)$ study of H_2 at large momentum transfer, Phys. Rev. A **90**, 052711 (2014).

[40] E. Wang, X. Shan, Q. Tian, J. Yang, M. Gong, Y. Tang, S. Niu, and X. Chen, Imaging molecular geometry with electron momentum spectroscopy, Sci. Rep. **6**, 39351 (2016).

[41] Z. Zhang, X. Shan, T. Wang, E. Wang, and X. Chen, Observation of the Interference Effect in Vibrationally Resolved Electron Momentum Spectroscopy of H_2, Phys. Rev. Lett. **112**, 023204 (2014).

[42] Y. Tang, X. Shan, S. Niu, Z. Liu, E. Wang, N. Watanabe, M. Yamazaki, M. Takahashi, and X. Chen, Electron momentum spectroscopy investigation of molecular conformations of ethanol considering vibrational effects, J. Phys. Chem. A **121**, 277 (2017).

[43] M. Yamazaki, K. Oishi, H. Nakazawa, C. Zhu, and M. Takahashi, Molecular Orbital Imaging of the Acetone S_2 Excited State using Time-Resolved $(e,2e)$ Electron Momentum Spectroscopy, Phys. Rev. Lett. **114**, 103005 (2015).

[44] M. Yamazaki, Y. Tang, and M. Takahashi, Ionization propensity and electron momentum distribution of the toluene S_1 excited state studied by time-resolved binary $(e,2e)$ spectroscopy, Phys. Rev. A **94**, 052509 (2016).

[45] K. A. Kouzakov, Y. V. Popov, and M. Takahashi, Laser-assisted electron momentum spectroscopy, Phys. Rev. A **82**, 023410 (2010).

[46] H.-C. Shao and A. F. Starace, Time-resolved ultrafast electron $(e,2e)$ momentum spectroscopy, Phys. Rev. A **87**, 050701(R) (2013).

[47] H.-C. Shao and A. F. Starace, Imaging population transfer in atoms with ultrafast electron pulses, Phys. Rev. A **94**, 030702(R) (2016).

[48] P. Eisenberger and P. M. Platzman, Compton scattering of x rays from bound electrons, Phys. Rev. A **2**, 415 (1970).

[49] M. Grosser, J. M. Slowik, and R. Santra, Attosecond x-ray scattering from a particle-hole wave packet, Phys. Rev. A **95**, 062107 (2017).

[50] M. Gell-Mann and M. L. Goldberger, The formal scattering theory, Phys. Rev. **91**, 398 (1953).

[51] I. E. McCarthy, Distorted-wave Born and impulse approximations for electron-atom ionisation, Aust. J. Phys. **48**, 1 (1995).

[52] K. Bartschat and M. J. Kushner, Electron collisions with atoms, ions, molecules, and surfaces: Fundamental science empowering advances in technology, Proc. Natl. Acad. Sci. USA **113**, 7026 (2016).

[53] Y. Miyake, M. Takahashi, N. Watanabe, Y. Khajuria, Y. Udagawa, Y. Sakai, and T. Mukoyama, Examination of $(e,2e)$ scattering models by comparison of momentum profiles of noble gases between experiment and theory, Phys. Chem. Chem. Phys. **8**, 3022 (2006).

[54] H.-C. Shao and A. F. Starace, Energy-resolved coherent diffraction from laser-driven electronic motion in atoms, Phys. Rev. A **96**, 042706 (2017).

[55] V. P. Krainov, H. R. Reiss, and B. M. Smirnov, *Radiative Processes in Atomic Physics* (John Wiley & Sons, Inc., New York, 1997).

[56] C. J. Joachain, N. J. Kylstra, and R. M. Potvliege, *Atoms in Intense Laser Fields* (Cambridge University Press, New York, 2012).

[57] F. Eholtzky, A. Jaroń, and J. Z. Kamiński, Electron-atom collisions in a laser field, Phys. Rep. **297**, 63 (1998).

[58] H.-C. Shao and A. F. Starace, Imaging electronic motions in atoms by energy-resolved ultrafast electron diffraction, Phys. Rev. A **90**, 032710 (2014).

[59] J. S. Melinger, S. R. Gandhi, A. Hariharan, D. Goswami, and W. S. Warren, Adiabatic population transfer with frequency-swept laser pulses, J. Chem. Phys. **101**, 6439 (1994).

[60] N. V. Vitanov, T. Halfmann, B. W. Shore, and K. Bergmann, Laser-induced population transfer by adiabatic passage techniques, Annu. Rev. Phys. Chem. **52**, 763 (2001).

[61] F. Herman and S. Skillman, *Atomic Structure Calculations* (Prentice-Hall, Inc., Englewood Cliffs, NJ, 1963).

[62] H. A. Bethe and R. W. Jackiw, *Intermediate Quantum Mechanics*, 2nd ed. (W. A. Benjamin, New York, 1968).

[63] J. Gillot, A. Gauguet, M. Büchner, and J. Vigué, Optical pumping of a lithium atomic beam for atom interferometry, Eur. Phys. J. D **67**, 263 (2013).